On the Aerodynamics Performance of MotoGP Wings

João Gaspar Cardoso Coelho da Silva
joao.gaspar.da.silva@ist.utl.pt

Instituto Superior Técnico, Universidade de Lisboa, Portugal

November 2019

Abstract

This dissertation aims to investigate the aerodynamic performance of the MotoGP wings.

In order to determine the flow field and aerodynamic characteristics of these wings, the Reynolds Averaged Navier-Stokes equations were solved with SST version of the $\kappa - \omega$ turbulence model and the transition model $\gamma - Re_\theta$, supported by the commercial software Starccm+.

Firstly, through the analysis of a symmetric airfoil, NACA0012, it was possible to observe a high dependence of the transition models on the numerical solutions.

Secondly, the dynamic analysis was performed to estimate the possible influence of the MotoGP prototypes accelerations and decelerations in the airfoil aerodynamic characteristics. The deviation of the numerical results from the dynamic analysis was considered negligible, the reason why a quasi-steady approach is sufficient.

Finally, three-dimensional analyses of different MotoGP wings configurations were performed with the NACA23015. From the numerical results, it was concluded that the three-dimensional effects highly influence the finite wings aerodynamic characteristics.

Keywords: CFD, MotoGP Wings, RANS, $\gamma - Re_\theta$ transition model, Closed Wings

1. Introduction

Grand Prix Motorcycle Racing, also known as MotoGP, is the premier class of motorcycle road racing events held on road circuit. For this reason, this competition has always been the stage of important developments. Race after race, manufacturers test new technologies looking forward to increase the prototypes performances. In consequence, over the last few years in MotoGP, riders struggle to handle these prototypes due to an excessive increase of the engine power. This excessive power motivates the front wheel loss of contact with the ground during acceleration, phenomenon known as front-end-lift.

Throughout the years, the MotoGP prototypes integrated different solutions to avoid the front-end-lift. Concerning aerodynamics, the solution was attaching downforce components all over the motorcycle fairings. The idea behind these wings is to produce enough downforce to overcome the inertia forces during acceleration. This way the engine power cut will be delayed increasing the power delivery to the rider.

The scope subject in this dissertation is to determine the performance of those wing aspiring to open a door in the study of different aerodynamic solutions to improve the motorcycle performance.

1.1. State of the Art

The flow around motorcycle side-wings occurs at moderate Reynolds numbers. Therefore, the boundary layer formed on the near wall region can be either laminar or turbulent.

Different studies were performed around airfoils at this regime showing accurate results using the Reynolds-averaged Navier–Stokes (RANS) solver with the SST $\kappa-\omega$ turbulence model and the $\gamma-Re_\theta$ transition model, from [19], [8] and [9]. One of the airfoils widely studied in these regimes is the NACA0012, with different numerical results, from [19] and experimental data available in [16] and [15]. Regarding the available information, at a first stage the side-wings will be studied in these regime with the NACA0012.

When it comes to subsonic velocities the wing characteristics can be highly sensitive to velocity variations, observed in [11], [18], [12] and [4]. For the present dissertation the wings experience either accelerations, decelerations and pitching motion during a full lap on a circuit. Concerning this transient mechanisms, one of the main goals in this dissertation is to determine if the quasi-steady simulations are closer or not to the unsteady simulations.

Lastly, this dissertation will study the three-dimensional effects over a finite-wing. The Mo-

toGP side-wings due to regulation geometric constrains are within the low aspect ratio wings. As a consequence, the three-dimensional effects tend to be highly intense, decreasing the substantially the wing performance, from [2] and [7].

1.2. Objectives

The two main concerns of this dissertation regards the transient and three-dimensional effects influence on the side-wings performance. In order to obtain an answer to these problems this thesis includes the following studies:

1. Include a transition model to simulate the flow with RANS
2. Obtain the lift and drag coefficients for the selected airfoil sections
3. Determine if unsteady simulations are required or a quasi-steady approach is sufficient to determine the airfoil properties.
4. Investigate the aerodynamics forces for the finite wings applied in MotoGP

2. Problem Definition

2.1. Flow Governing Equations

The problem at scope is an external isothermal incompressible flow over a wing, governed by the Navier-stokes equations described below:

$$\begin{cases} \dfrac{\partial u_i}{\partial x_i} = 0 \\ \dfrac{\partial u_i}{\partial t} + u_j \dfrac{\partial u_i}{\partial x_j} = \dfrac{\partial \tau_{ji}}{\partial x_j} - \dfrac{1}{\rho}\dfrac{\partial p}{\partial x_i} \end{cases} \tag{1}$$

Where u_i is the velocity in direction x_i, t the time, τ_{ij} the viscous stress tensor and p the pressure. The viscous shear stresses represent the internal friction force of fluid layers against each other and is given below:

$$\vec{\tau_{ij}} = \nu \left(\frac{\partial u_i}{\partial x_j} + \frac{\partial u_j}{\partial x_i} \right) \tag{2}$$

2.2. Reynolds range

The existence of a solid body within the viscous fluid domain leads to the emergence of a boundary layer (BL) near the wall region. This small region is highly dependent on the interaction between the diffusion and convection. The dimensionless number that controls this interaction is the Reynolds number in equation 3 which balances the inertial over the viscous forces.

$$Re = \frac{U_e L}{\nu} \tag{3}$$

Where U_e is the income flow velocity, L a length scale and ν the fluid kinematic viscosity.

For the motorcycle velocity ranges and the wing size depicted in the previous section, these wings range Reynolds between $2.4 \cdot 10^5$ and $1 \cdot 10^6$. This range corresponds to the critical region where the BL is affected by transition mechanisms.

2.3. Case study 1

In the present section will be estimated the order of magnitude of the fluid inertial forces during accelerations and decelerations.

Objects and fluids can not occupy the same physical space simultaneously. As a consequence, when a object changes its velocity deflects the surrounding fluid volume. This displaced mass is known as added mass or virtual mass and can be responsible for the adding of a significant amount of inertia to a system. This inertia is written in equation 4.

$$F_{am} = \rho V_{fluid} \frac{\partial U}{\partial t} \tag{4}$$

Where V_{fluid} is the displaced volume.

In table 2.3 is presented the magnitude order of this fluid inertia forces for accelerations and decelerations performed by the motorcycle.

	m_{11} $[kg]$	a $[m/s^2]$	$F_{acc}[N]$
Acceleration	$5.3 \cdot 10^{-4}$	7	$3.7 \cdot 10^{-3}$
Deceleration	$5.3 \cdot 10^{-4}$	10	$5.3 \cdot 10^{-3}$

Table 1: Added mass and fluid inertia under acceleration and deceleration. m_{11} stands for the added mass of a ellipse moving in the streamwise direction.

2.4. Case study 2

From a dynamic point of view, motorcycle can be considered as a rigid body connected to the wheels by an elastic system, [1]. Any inertia force that disturbs the sprung mass will cause a pitch and bounce motion to it. The side-wings racing in MotoGP are attached to this sprung mass and consequently share the same dynamic behaviour.

In pitching motion three mechanisms acting on the airfoil are contributing to the global forces: the dynamic stall, the vortex shedding and the added mass. This case study aims to determine whether these mechanisms have an important role on the wing properties for the pitching frequencies on track conditions.

2.4.1 Dynamic stall and vortex shedding

The Strouhal number is a dimensionless number describing oscillating flow mechanisms. When it comes to analysis of a pitching airfoil, the Strouhal number is given by equation 5.

$$St = \frac{2 f h_0}{U_e} \tag{5}$$

Where f is the frequency of pitching, the h_0 is the maximum displacement traversed by the trailing edge and U_e the income velocity.

The side-wings can experience two different scenarios during a complete lap on a circuit:a sudden variation after braking or accelerating, corresponding to highest AoA variations, or an intermittent suspension oscillation with lower AoA variations, corresponding to the shock absorber energy dissipation. In table 2.4.1 are presented the typical working frequencies, amplitudes and strouhal numbers for the lower and higher amplitudes at a velocity of $30m/s$ assuming that the airfoil is rotating over 25% of the chord.

	$f[Hz]$	AoA_{max} [°]	St
HA	0.6	2	$2.2 \cdot 10^{-4}$
LA	3.1	0.5	$2.7 \cdot 10^{-4}$

Table 2: Pitching characteristics for the motorcycle side-wings. LA stands for low amplitudes and HA for higher amplitudes

2.4.2 Added mass

In this section the inertial forces during pitching motion will be determined. From [14] the angular acceleration will be approximated to a linear acceleration at the airfoil trailing edge linear acceleration, and is written as:

$$a_{TE,p} = -r\alpha_0\omega^2 sin(\omega t) \tag{6}$$

where r is the radius concerning the pitching rotation center, the α_0 is the airfoil AoA ω the angular frequency and t the time. The maximum of equation 6 is achieved when $\alpha_0 = \frac{h_0}{r}$ where the h_0 is the amplitude vertical distance measured on the trailing edge from [14].

The inertia forces associated with the pitching motion from equation 4 are depicted in table 2.4.2.

	m_{33} $[kg]$	a $[m/s^2]$	$F_{acc}[N]$
HA	$1.1 \cdot 10^{-3}$	$8.2 \cdot 10^{-2}$	$9.2 \cdot 10^{-5}$
LA	$1.1 \cdot 10^{-3}$	0.5	$5.8 \cdot 10^{-4}$

Table 3: Added mass and inertial forces under pitching motion. LA stands for low amplitudes, HA for higher amplitudes, m_{11} for the added mass of an ellipse pitching.

3. Mathematical Models and Numerical Methods

3.1. Reynolds Averaged Navier-Stokes Equations

Reynolds proposed a statistical approach to solve the NSE. Considering that turbulent flow is characterized by the fluctuation of a property ϕ_i, the statistical value of this property is expressed by the sum of a mean component ($\overline{\phi_i}$) and a fluctuation component (ϕ_i'), equation 7.

$$\phi_i = \overline{\phi_i} + \phi_i' \tag{7}$$

Applying this composition to the NSE, the RANS can be written as:

$$\frac{\partial \bar{u_i}}{\partial x_i} = 0 \tag{8}$$

$$\frac{\partial \overline{u_i}}{\partial t} + \overline{u_j}\frac{\partial \bar{u_i}}{\partial x_j} + \frac{\partial}{\partial x_j}\left(\overline{u_i' u_j'}\right) = \nu\frac{\partial^2 \bar{u_i}}{\partial x_j^2} - \frac{1}{\rho}\frac{\partial \overline{p}}{\partial x_i} \tag{9}$$

Comparing equations 9 and the NSE 1, the average process results in the emergence of a new term, the Reynolds stresses $\overline{u_i' u_j'}$. The Reynolds stress tensor introduces new variables to the system of equations which have no additional equations to be determined. As a result, the RANS becomes an undetermined system and depends upon additional equations.

3.2. Turbulence Models

The Reynolds stress is the main concern of turbulence in engineering problems. Boussines proposed an approximation to the Reynolds stress tensor by assuming a direct proportionality to the velocity gradients, as shown in equation 10.

$$-\overline{u_i' u_j'} = \nu_t\left(\frac{\partial \overline{u_i}}{\partial x_j} + \frac{\partial \overline{u_j}}{\partial x_i}\right) \tag{10}$$

Where ν_t is the eddy-viscosity.

Different turbulence models use the Boussines assumption to calculate the eddy viscosity. The Menter shear stress transport $\kappa - \omega$ (SST $\kappa - \omega$), from [17] and [3], is the widely used turbulence model for these applications which uses two blended models: The $\kappa - \epsilon$ model, developed by Jones and Launder [3] and the $\kappa - \omega$, developed by Wilcox [3]. The SST $\kappa - \omega$ is a two equation model that uses the Boussines assumption to calculate the eddy viscosity. This model which uses blending functions to change between the $\kappa - \omega$ and the $\kappa - \epsilon$ depending on the wall distance. These equations can be found in [3].

3.3. Transition Models

The turbulence models, as SST $\kappa - \omega$, were not developed to predict transition,[13] and [6]. This model estimates the transition location based on the model turbulence production. The coupling of a transition model aims to control the turbulence production locally. The transition model used on this dissertation is $\gamma - Re_\theta$, a two equations model, with one transport equation for the intermittency γ, which triggers transition in BL and another one for the local momentum thickness Reynolds Re_θ, which

controls the transition location. The corresponding equations can be found in [10]

The transition model requires the calculation of the shear stress at the wall by definition at the viscous sub-layer [10]. As a result, the first element near the wall region should be catched within this layer. Typically ,for a proper modelling, the dimensionless wall distance y^+ of the first element near the wall should be lower than one, [10].

3.4. Wall Treatment

At this stage, it is already known that flow is highly dependent on the transition process and consequently the near wall region must be managed carefully. From the previous section, the transition model requires the dimensionless distance to the wall, equation 11, to be lower than one.

$$y^+ = \frac{u_\tau y}{\nu}; \tag{11}$$

$$u_\tau = \sqrt{\frac{\tau_w}{\rho}} = U_e\sqrt{\frac{C_f}{2}} \tag{12}$$

From the relations 11 and friction velocity 12 the effective dimension of the first element near the wall is given below:

$$\frac{y_2}{c} < \frac{1}{Re_{chord}}\sqrt{\frac{2}{C_f}} \tag{13}$$

The minimum element size is given for the maximum friction coefficient (C_f) value over the airfoil, corresponding to the transition to turbulent location. As a first approach, it was performed a simulation in XFoil6.99 to a NACA0012 for an average Reynolds number $Re = 5 \cdot 10^5$ at a 0º AoA. For a transition location at 79% of the chord the $C_f \approx 3.5 \cdot 10^{-3}$. As a result, from equation 13, the minimum size of the first element near the wall region should be lower than $8.43 \cdot 10^{-6} m$.

3.5. Discretization Schemes and Solution Algorithms

The selected discretization schemes are detailed in table 3.5 with second order schemes in space discretization and first order in time. Besides the accuracy of a finite volume solution being related to the manner in which the flow equation is discretized, it is also important to establish how they were solved. The solution of the numerical results was accomplished using a segregated iterative method based on the SIMPLE algorithm [5].

4. 2D-RANS NACA0012

In this section a parametric analysis to an airfoil NACA0012 will be performed using the commercial software Starccm+ 13.06.

	Scheme
Convection - $\gamma - Re_\theta$	2nd-order upwind
Convection - $SST\ \kappa - \omega$	2nd-order upwind
Convection - Momentum	2nd-order upwind
Unsteady $\left(\frac{\partial}{\partial t} \neq 0\right)$	1nd-order Implicit

Table 4: Discretization Schemes applied to the NSE to solve the convection flow problem

4.1. 2D-Grid

The domain and grid definition represent an important step to accurately determine the final solution of the problem. The present grid is a quadrilateral Multi-block grid, figure 1(a), with a near wall body-fitted C-Mesh structured grid, figure 1(b). In addition, the prismatic layer near the wall region was set to $20mm$ thick and the elements growth rate followed a geometric progression with a stretching factor of 1.2. As the blocks stepped aside from this region, the grid remains growing with the same rate but with a different cells sizes, ensuring that the transition between blocks is smooth. The proper

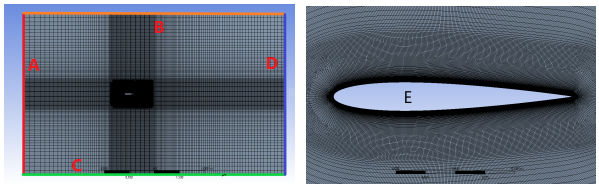

(a) Multi-grid block grid division around NACA0012 (b) Near wall body-fitted C-Mesh around NACA0012

Figure 1: Two-dimensional block grid around the NACA0012

domain size will be determinant to an accurately measurement of the airfoil properties. After several attempts the selected domain characteristics are presented in table 4.1.

	A	B,C	D	E
BC	Velocity Imposed		P_{outlet}	No slip
LED	$10 \cdot c$	$8 \cdot c$	$15 \cdot c$	-

Table 5: Domain size and boundary conditions. where c stands for the chord length and the letters A,B,C,D and E are identified in figure 1. BD stands for boundary conditions and LED to leading edge distance

4.1.1 Discretization Error Assessment

To estimate the discrtization error of the grid developed was used the Richardson extrapolation:

$$\delta_{RE} = \phi_i - \phi_0 = \alpha h_i^p \tag{14}$$

Where p is the order of convergence, ϕ is the quantity to evaluate, h_i the relative grid spacing, α a constant and δ_{RE} the discretization error.

To close the equation 14 are needed at least three numerical solutions from three different grids. In the present work, the other two solutions were taken from more sparse and thinner grids with a refinement reason of 1.4 in x and y direction. The discretization errors were measured for the pressure drag coefficient, lift coefficient and pressure coefficient, as depicted in the table 4.1.1.

	C_l	$C_{dp} \cdot 10^3$	$C_{df} \cdot 10^3$
Grid 1	0.216	3.557	3.776
Grid 2	0.217	3.417	3.781
Grid 3	0.217	3.374	3.782
δ	$5.17 \cdot 10^{-4}$	$4.23 \cdot 10^{-5}$	$1.88 \cdot 10^{-6}$

Table 6: Dicretization errors associated with the different properties of the numerical solution from the structured mesh for $Re = 3.6 \cdot 10^5$ and 2° AoA (NACA0012).

4.2. Flow characteristics

At moderate Reynolds numbers, different transition mechanisms are responsible for determination of flow characteristics. In this problem, a separation bubble motivates the boundary layer transition. The separation bubble phenomenon presented in this section is caused by an adverse pressure gradient from the airfoil shape action on a laminar boundary layer. Since laminar boundary layer is less diffusive than turbulent ones, it is more likely to separate. After separation, free-shear layer promotes the boundary-layer transition and afterwards, due to high diffusivity of turbulent boundary layers, it reattaches to the surface. Throughout this section was determined the influence of different angles of attack, Reynolds number and inlet condition on the separation bubble process.

Increase airfoil angle of attack is equivalent to increase adverse pressure gradient on the suction side. Given the fact that separation mechanism has a direct relation with the boundary layer separation, the separation bubble on the suction side moves towards to the leading edge as the adverse pressure gradient increases, i.e. angle of attack increase, illustrated in figure 2(a). The next experiment looks for the influence of different velocities imposed at the inlet. The inlet velocity increase results in an increase of the momentum close to the wall. Consequently, the free-shear layers will cause a quicker transition of the laminar separation and consequently an early reattachment. As a result, the Reynolds number increases shrank the separation bubble, illustrated in figure 2(b).

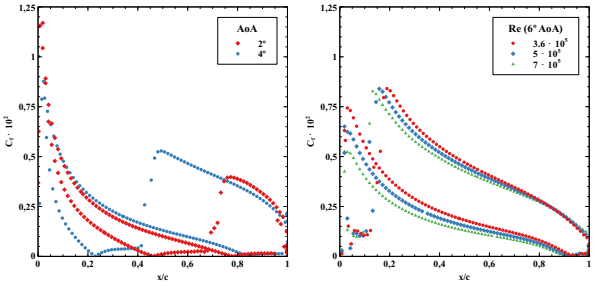

(a) NACA0012 $|C_f|$ distribution to 2° and 4° AoA for $Re = 5 \cdot 10^5$

(b) NACA0012 $|C_f|$ distribution for 6° AoA along the dimensionless chord for $Re = 3.6 \cdot 10^5, 5 \cdot 10^5, 7 \cdot 10^5$

Figure 2:

To determine the influence of the income flow turbulence levels, were chosen angles of attack close to the stall angle of attack. The turbulence levels were controlled by the viscosity ratio values between 0.1 and 0.01. From the numerical results was concluded that the decrease of the free-shear layers turbulence near the stall region can cause different separation mechanisms. If the turbulence levels are too low, the laminar boundary layer after separation is not able to transit to turbulent causing a massive laminar separation with a sudden decrease of the airfoil lift, as illustrated in figure 3(a).

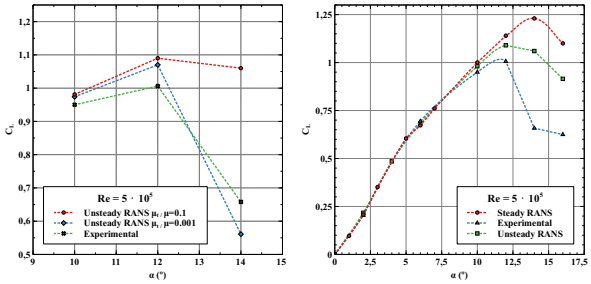

(a) NACA0012 lift coefficient of experimental data and numerical results at $Re = 5 \cdot 10^5$. (Experimental data taken from [16] and [15])

(b) NACA0012 lift coefficient of experimental data and numerical results at $Re = 5 \cdot 10^5$. (Experimental data taken from [16] and [15])

Figure 3:

4.3. Airfoil properties

The characteristic properties of the airfoil, as C_l and C_d, are mainly dependent on the Reynolds number, airfoil shape and AoA. In these sections will be analysed the NACA0012 for three Reynolds numbers, $Re = 3.6 \cdot 10^5, 5 \cdot 10^5, 7 \cdot 10^5$, until the stall incidence.

The numerical analysis started with a steady approach since the problem at scope, was expected to have a steady solution. However, this bubble, presented in section 4.2, showed a highly unstable be-

haviour not allowing the residuals and properties to stabilize. As a consequence, convergence was only possible with a highly under-relaxation of the solver and for higher AoA with an increase of the inlet turbulence condition to force the bubble reattachment.

Since the numerical results for the steady analysis plotted in figure 3(b) deviates from experimental data for higher AoA was performed an unsteady analysis that showed up to be less time consuming and easy to converge.

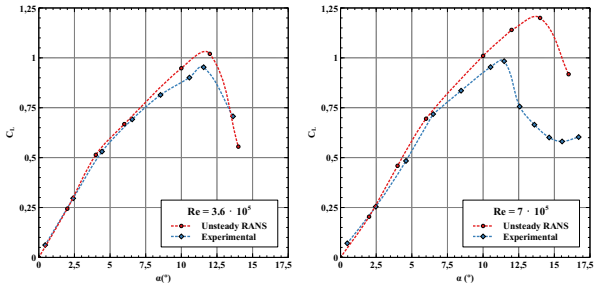

(a) NACA0012 lift coefficient of experimental data and numerical results at $Re = 3.6 \cdot 10^5$. (Experimental data taken from [16] and [15])

(b) NACA0012 lift coefficient for experimental data and numerical results at $Re = 7 \cdot 10^5$. (Experimental data taken from [16] and [15])

Figure 4:

As illustrated in the same plot for the unsteady numerical results for higher AoA the numerical solutions continued to deviate from the experimental data although the stall angle of attack predicted by the unsteady solver is closer to the experiment. For Reynolds numbers of $Re = 3.6 \cdot 10^5$ and $7 \cdot 10^5$ the same deviations were observed, as illustrated in figures 4(a) and 4(b) respectively.

4.4. Acceleration Analysis to NACA0012 (Case Study 1)

In this section will be shown the results of accelerating and decelerating an airfoil at 6° and 10° respectively with the physic conditions described in section 2.3. From the C_L and C_D plots in figures 5(a) and 5(b) was concluded that the differences between the steady and transient processes were at most 2%, thus concluding that the transient process does not affect the equilibrium of global forces. The result was expected since the inertial forces for this case study were three to five orders of magnitude below the drag and lift forces.

4.5. Frequency Analysis to NACA0012 (Case Study 2)

In this section will be shown the results of pitching an airfoil between 6° and 10° with the physic conditions described in section 2.4.

Firstly, neither the vortex shedding nor the dynamic stall were verified for the problem angular frequencies and AoA amplitudes. This result was

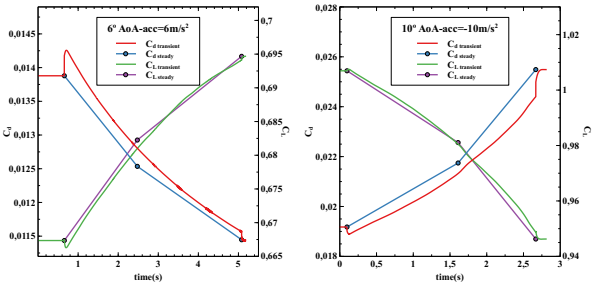

(a) NACA0012 lift and drag coefficient for a transient velocity condition and a steady state solutions

(b) NACA0012 lift and drag coefficient for a transient velocity condition and a steady state solutions

Figure 5:

already expected from [4] since both mechanisms take place at higher Strouhal numbers and angles of attack.

Similarly to the first case study, the lift coefficient lies within the steady solution for angles of attack of 6° and 10° with negligible deviations, as illustrated in figure 6(a). However, it is observed a deviation on the drag coefficient. Once again, this deviation could be explained by the fluid inertia forces acting on the airfoil during the change in the rotation direction.Nonetheless, for the dissertation goal, the deviation observed in C_d plot is not representative. Thereby, it will be assumed that the pitching motion does not influence the airfoil properties.

After performing both transient case studies, it was concluded that a quasi-steady approach is acceptable to proceed with further analysis.

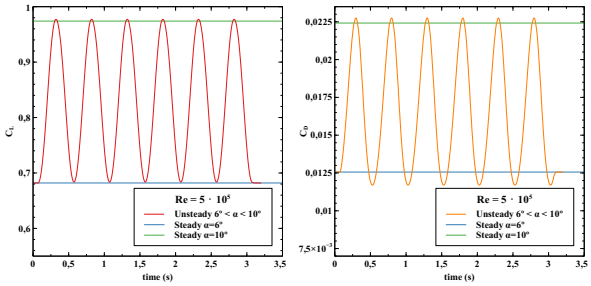

(a) NACA0012 lift coefficient for a transient angular frequency condition and a steady state solutions for $Re = 5 \cdot 10^5$

(b) NACA0012 drag coefficient for a transient angular frequency condition and a steady state solutions for $Re = 5 \cdot 10^5$

Figure 6:

5. 3D-RANS NACA23015

When it comes to the three-dimensional analysis, there is an additional effect concerning lift. Near the wing tip the air can move from the pressure side to the suction side. As a result, it is formed a tip-vortex that interferes with the streamwise flow.

This vortex effect over the wing is negligible as long as the wing-span over the wing-chord (aspect ratio) remains higher. As MotoGP regulation constrain the maximum wing-span, these wings end-up with low aspect ratio and highly prone to the three-dimensional effects. In short, the main concern through this chapter is to measure the influence of the three-dimensional effects over low aspect ratio wings.

5.1. Finite-Wing Analysis

As a first approach to the finite-wing analysis, in this section will be determined the properties of a wing without end-plate with symmetry condition on the wing-root. The wings studied are identical to the MotoGP wings with a wing chord length of $0.2m$ and a wing span of $0.2m$.

Either the separation bubble and the crosswise flow coming from the wing pressure side, are phenomena that change the streamwise velocity and consequently the shear stress at the wall. One of the techniques proposed in [2] to illustrate these effects is to plot the skin friction lines over the wing surfaces. These limiting flow lines not only illustrate the streamlines directions but also the boundary layer separation and reattachment zones.

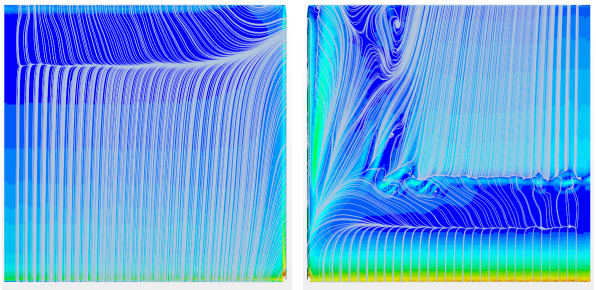

(a) Skin friction lines for the pressure side of the finite-wing with symmetry condition on the wing root for $Re = 3.6 \cdot 10^5$ and 6°AoA

(b) Skin friction lines for the suction side of the finite-wing with symmetry condition on the wing root for $Re = 3.6 \cdot 10^5$ and 6°AoA

Figure 7: Skin friction lines for the finite-wing with symmetry condition on the wing root for $Re = 3.6 \cdot 10^5$ and 6°AoA

From the Skin friction lines plotted in figure 7 are illustrated different patterns representative of the already discussed separation and reattachment regions. Firstly, is observed either on pressure and suction side, a region highly similar to the two-dimensional results. On the wing pressure side the flow is similar to the 2D numerical solutions in approximately 60% of the wing, as illustrated in figure 7(a). However, near the wing tip, since the flow is free to move from the pressure to the suction side, the limiting flow lines exhibit a slight deviation to the crosswise direction in almost 40% of the wing.

On the wing suction side in figure 7(b) the flow became more complex. Besides the region where the flow is similar to the 2D numerical solution, the crosswise velocity disturbs almost 40% of the wing-span. In this region can be observed different three dimensional separations due to secondary flows with spiral points reattachment and separation regions consequence of the tip-vortex. From

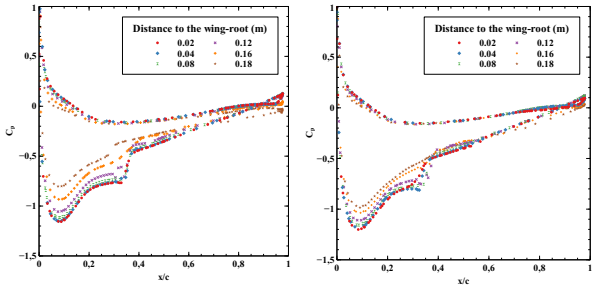

(a) C_P distribution in different sections along the span in the crosswise direction for the finite-wing with symmetry condition on the wing root for $Re = 3.6 \cdot 10^5$ and 6°AoA

(b) C_P distribution in different sections along the span in the crosswise direction for the wing with end-plate and no-slip condition on the wing root at $Re = 3.6 \cdot 10^5$ and 6°AoA

Figure 8:

the C_p plot in figure 8(a) for different wing sections in crosswise direction, is evident the tip-vortex perturbation with a sudden pressure loss on the sections near the wing-tip ($0.16m$ and $0.18m$). As long as the wing sections get closer to the wing root, the effect fades and the C_p increases.

5.2. Wing with end-plate

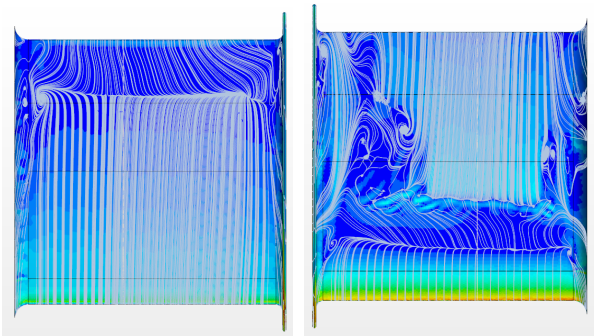

(a) Skin friction lines for the pressure side of the finite wing with end-plate at the tip for $Re = 3.6 \cdot 10^5$ and 6°AoA

(b) Skin friction lines for the suction side of the finite wing with end-plate at the tip for $Re = 3.6 \cdot 10^5$ and 6°AoA

Figure 9: Skin friction lines for the finite wing with end-plate at the tip for $Re = 3.6 \cdot 10^5$ and 6°AoA

In this section was performed an analysis to the same wing studied on the previous section but attached to a wall on the wing root and an end-plate

on the wing tip. Following the same technique used before, are plotted the skin friction lines over the wing surface as illustrated in figure 9.

On the wing pressure side the flow is similar to the 2D numerical solutions in approximately 90% of the wing, as illustrated in figure 7(a). This effect is due to the end-plate attachment on the wing tip that considerably reduced the crosswise velocity on the pressure side.

On the other hand, at the suction side near the end-plate the interaction between the tip-vortex and the secondary flows, have a massive impact over the streamwise flow. This secondary flow disturbs more than 30% of the streamwise flow over the wing span. As expected, the end-plate attachment at the wing tip increased the global wing pressure distribution. From the C_p plot in figure 8(b), and the skin friction lines in figure 9 the pressure increase is caused by a lower interference of the crosswise velocity on the pressure side. As a result, the wing properties increased substantially when compared to wings without end-plate.

5.3. MotoGP Case Study

In this section one of the box-wings set-ups racing in MotoGP will be discussed. The upper and lower wings cross section is a NACA23015 airfoil and the connecting wing is a NACA0006 airfoil. The AoA of both wings are identical and the distance between the upper and lower wings was set to half of a wingspan.

Following the same analysis of previous sections, on figure 10 are plotted the skin friction lines on the wing surfaces. Since the wings are too close from each other, the pressure communications on the outer side remain appreciable. As a result, it is observed in figure 10(a) and 10(b) a flow patter similar to the that on finite-wing without end-plate in figure 7.

Concerning the inner side of the box-wing, due to high proximity of the upper and lower wing, the flow pattern changed completely. From figure 10(d) on the upper wing, the laminar separation that took place at 10% of the chord due to the wings proximity is located at more than 50% of the chord. Similarly from figure 10(c) on the lower wing, the separation bubble changed its position on the opposite direction with an early laminar separation. As long as the gap increases, the interference decreases and the separation bubbles move forward to its initial position.

The flow interference illustrated on the limiting flow lines is a consequence of the flow acceleration at the inner side of the box-wing. The wings proximity works as a nozzle increasing the kinetic energy of the flowing medium at the expense of its pressure. As a result, the upper wing end-up more loaded than the lower one as illustrated on the C_p plot for both wings in figure 11. For this specific bow-wing configuration, besides the upper wing produces more downforce than the previous wings configurations, due to the flow interference the lower wing instead of producing downforce it starts to produce lift.

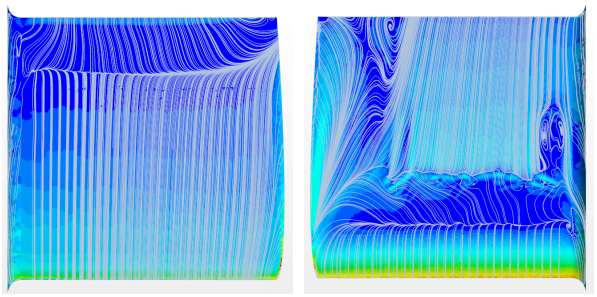

(a) Skin friction lines for the pressure side of the upper-wing

(b) Skin friction lines for the suction side of the bottom-wing

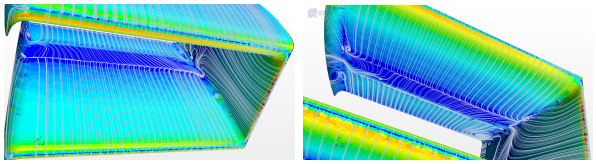

(c) Skin friction lines for the pressure side of the bottom-wing

(d) Skin friction lines for the suction side of the upper-wing

Figure 10: Skin friction lines for the close-wing with half span length distance at $Re = 3.6 \cdot 10^5$ and 6° AoA

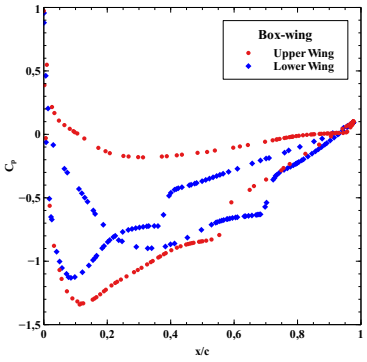

Figure 11: C_p distribution of a section not disturbed by crosswise velocities for the closed wing at $Re = 3.6 \cdot 10^5$ and 6°AoA

5.4. Final considerations

Concerning the low aspect ratio wings, it is now possible to state that independently of the set-up, the downforce loss caused by the upwash velocity is considerably high. It is also possible to state that, for the three different set-ups, the separation bubble is highly sensible to the three-dimensional effects

leading to changes in the flow characteristics and in the global wing properties as well.

The end-plate attachment to a finite wing substantially increases the lift coefficient, proving to be the most efficient way to produce downforce.

Lastly, the closed-wing results allow to infer that the high interference levels between wings decrease the global wing efficiency. However, if the space available through the motorcycle fairing constrains the total number of wings, then overlapping two wings may not be the most efficient way to produce downforce but at least it is a way to produce more downforce.

6. Conclusions

The main conclusions are:

- Firstly, throughout the dissertation the coupling transition model $\gamma - Re_\theta$ to solve the RANS equations showed to be crucial to reliably determine the flow characteristics and the wing properties under moderate Reynolds numbers. The turbulence model, by itself, was not able to predict the exact transition location, neither the separation bubble phenomenon.

- Either for steady or unsteady numerical results, the transition model showed a high sensibility to the inlet turbulence conditions. Consequently, to determine the wings properties accurately, it should be provided the information regarding turbulence.

- The separation bubble proves to have a key role in the flow features. Under the two-dimensional analysis were determined that near the stall region, this bubble can induce different stall mechanisms that depend on the freestream flow conditions. As a result, for safety reasons, when the motorcycle undergoes a deceleration, the wing angle of attack should be controlled to avoid the unstable effects of the wing stall.

- Concerning the transient process associated with motorcycle track behaviour, neither the acceleration nor the deceleration affected the airfoil properties. Likewise, the wing performance is not sensitive to the pitching motion regarding the motorcycle suspension frequencies.

- Regarding the finite-wing results, it can be stated that due to the span-length restriction from MotoGP regulation, the prototypes side-wings end-up highly prone to three-dimensional effect. As a result, the downforce of these wings decreases in more than 50% in contrast to higher aspect ratio wings.

- For the three set-ups depicted in this dissertation, the attachment of an end-plate proved to be the more efficient way to produce downforce. Although, since the MotoGP regulation forbids these wings as a safety feature, the manufactures are restricted to design box-wings. For the studied configuration of two overlapped wings, besides the interferences between them have decreased the set-up efficiency, the global downforce increased 30% about the wing with end-plate.

7. Future work

Concerning the three-dimensional results, different subjects would be interesting to explore in the future. In the present dissertation, the motorcycle fairing was approximated to a flat plate. However, these wings are attached to a region where the fairing shape induces a favorable pressure gradient to the flow. It would be worthwhile to determine how different fairing shapes can affect the wing properties due to the flow acceleration in the neighborhood of the motorcycle fairing.

In addition, the three-dimensional analysis of different wing configurations opened doors to different ideas to increase the MotoGP box-wings performance. Since MotoGP wings are constrained to the available space on the motorcycle, it is required to study a way to decrease the flow interference between the upper and lower wing. As a future work is suggested to optimize box wings for different configurations, changing different parameters to decrease the flow interference. To increase the global downforce is required to decrease the influence of the flow acceleration on the lower wing. That can be handled by managing the angles of attack of upper and lower wing, the gap, or the position between them.

References

[1] V. Cossalter. *Motorcycle Dynamics 2nd Edition.* 2006.

[2] V. de Brederode. *Aerodinâmica Incompressível Fundamentos.* 1997.

[3] Z. T. Equation and T. Models. Two-Equation. 1993.

[4] J. Guerrero. Aerodynamics of Flapping Flight. *Numerical Simulation of the unsteady Aerodynamics of flapping flight*, pages 7–33, 2009.

[5] C. Hirsch. *Numerical Computation of Internal & External Flows By C. Hirseh (Vol.-2).* 1990.

[6] F. Joel and L. Gamboa. Numerical Analysis of an Wing Sail Aerodynamic Characteristics Using. 2010.

[7] O. F. Low-aspect ratio, T. O. The, N. F. Copy, P. Retli, N. T. O. Coo, and N. Aeronautics. Technical note. (July 1961), 2019.

[8] A. Marta. Hydrodynamic analysis of a slalom fin of windsurf board. (December), 2018.

[9] R. Miguel and A. Lopes. Calculation of the flow around hydrofoils at moderate Reynolds numbers. (December), 2015.

[10] Robin Blair Langtry. A Correlation-Based Transition Model using Local Variables for Unstructured Parallelized CFD codes. 2006.

[11] H. Roohani. *Aerodynamic effects of accelerating objects in air*. Number September. 2010.

[12] M. E. Rosti, M. Omidyeganeh, and A. Pinelli. Video: Dynamic stall of an aerofoil in ramp-up motion. In *69th Annual Meeting of the APS Division of Fluid Dynamics - Gallery of Fluid Motion*. American Physical Society, nov 2016.

[13] C. L. Rumsey and P. R. Spalart. Turbulence model behavior in low reynolds number regions of aerodynamic flowfields. *AIAA Journal*, 47(4):982–993, 2009.

[14] M. Saif, U. Khalid, I. Akhtar, and N. I. Durrani. Aerodynamic Characteristics of Pitching and Plunging Airfoils at Low Reynolds Number. pages 1–28, 2014.

[15] R. E. Sheldahl and P. C. Klimas. Sandia_Lab_Data. 1981.

[16] B. H. a. Smith and R. F. Schaefer. for Aeronautics Technical Note 2074. (April):0–10, 1950.

[17] H. Versteeg and W. Malalasekera. *An Introduction to Computational Fluid Dynamics*, volume M. 2007.

[18] Z. J. Wang. Vortex shedding and frequency selection in flapping flight. *Journal of Fluid Mechanics*, 410:323–341, 2000.

[19] J. Winslow, H. Otsuka, B. Govindarajan, and I. Chopra. Basic Understanding of Airfoil Characteristics at Low Reynolds Numbers (104–105). *Journal of Aircraft*, 55(3):1050–1061, 2017.